PNAS RESEARCH ARTICLE | CHEMISTRY

Toward a quantitative interfacial description of solvation for Li metal battery operation under extreme conditions

John Holoubek[a,1], Kunpeng Yu[a], Junlin Wu[b], Shen Wang[a], Mingqian Li[a], Hongpeng Gao[b], Zeyu Hui[a], Gayea Hyun[a], Yijie Yin[b], Anthony U. Mu[a], Kangwoon Kim[a], Alex Liu[a], Sicen Yu[b], Tod A. Pascal[a,b,c], Ping Liu[a,b,c,1], and Zheng Chen[a,b,c,1]

Edited by Alexis Bell, University of California, Berkeley, CA; received June 25, 2023; accepted August 17, 2023

The future application of Li metal batteries (LMBs) at scale demands electrolytes that endow improved performance under fast-charging and low-temperature operating conditions. Recent works indicate that desolvation kinetics of Li^+ plays a crucial role in enabling such behavior. However, the modulation of this process has typically been achieved through inducing qualitative degrees of ion pairing into the system. In this work, we find that a more quantitative control of the ion pairing is crucial to minimizing the desolvation penalty at the electrified interface and thus the reversibility of the Li metal anode under kinetic strain. This effect is demonstrated in localized electrolytes based on strongly and weakly bound ether solvents that allow for the deconvolution of solvation chemistry and structure. Unexpectedly, we find that maximum degrees of ion pairing are suboptimal for ultralow temperature and high-rate operation and that reversibility is substantially improved via slight local dilution away from the saturation point. Further, we find that at the optimum degree of ion pairing for each system, weakly bound solvents still produce superior behavior. The impact of these structure and chemistry effects on charge transfer are then explicitly resolved via experimental and computational analyses. Lastly, we demonstrate that the locally optimized diethyl ether-based localized-high-concentration electrolytes supports kinetic strained operating conditions, including cycling down to −60 °C and 20-min fast charging in LMB full cells. This work demonstrates that explicit, quantitative optimization of the Li^+ solvation state is necessary for developing LMB electrolytes capable of low-temperature and high-rate operation.

battery | electrolyte | solvation | charge-transfer

Li-ion batteries (LIBs) are a foundational technology for modern portable electronics and electric vehicles. Though continual advancement of the energy density of these systems has been achieved through consistent advances in cell engineering, the next step in such advancement requires the advent of fundamentally new battery chemistries (1). Among the prospective candidates, Li metal batteries (LMBs) are among the most promising, where the graphite anode (372 mAh g^{-1}) is replaced with Li metal (3,860 mAh g^{-1}) (2–4). In addition to design challenges aimed at mitigating parasitic reactivity and volume change, LMBs must also adhere to the same or similar use conditions as next-generation LIBs (5–8). Namely, the energy output, Coulombic efficiency (CE) -defined cyclability, and safety of LMBs must be ensured under kinetically strained operation conditions such as fast-charging and low-temperature operation (9–11).

Despite these requirements, progress for both LIBs and LMBs has been limited in part due to a somewhat imprecise understanding of the effect of and interplay between various kinetic limiting factors during battery operation. The various kinetic barriers experienced by a Li^+ ion during LIB and LMB operation are generally grouped as follows: 1) transport of Li^+ through the bulk electrolyte, 2) Li^+ desolvation at the electrode/electrolyte interface, 3) migration of Li^+ through the solid-electrolyte-interface (SEI), and 4) diffusion of Li^+ through the bulk electrode (12–14). As the first 3 of these contributors are defined by the electrolyte, the development of improved electrolyte chemistries is considered a foremost strategy to improve battery performance under kinetic strain (11, 15). Of note, substantial improvements in ionic conductivity have been made through the advent of reduced viscosity solvents (for LIBs) (16–19) and SEI transport through the introduction of fluorinated compounds and high-concentration solutions (20–25). The development of strategies to improve the desolvation penalty is significantly less available due to its inherent fundamental complexity and difficulties associated with its direct characterization and deconvolution from other processes. Considering the latter, the growing literature consensus that desolvation dominates low-temperature (e.g., <−30 °C) performance provides an opportunity to study and develop approaches targeting this process (12, 14, 26, 27).

Significance

The liquid electrolytes that underpin most electrochemical systems consist of salt(s) and solvent(s), that once dissolved form distinct "solvation" structures at the molecular level. This structure has dramatic effects on the kinetics of Li metal batteries. While recent reports suggest that highly ion-paired solvation states are desirable, this guidance is ultimately qualitative. In this work, we experimentally and computationally study a series of sequentially modulated electrolytes, which demonstrate superior kinetics at compositions slightly diluted away maximum ion pairing. These findings advance a more quantitative relationship between solvation and kinetics and provide actionable guidance for the design of low-temperature and fast-charging Li metal batteries.

Author affiliations: [a]Department of NanoEngineering, University of California San Diego, CA 92093; [b]Program of Materials Science and Engineering, University of California San Diego, CA 92093; and [c]Sustainable Power and Energy Center, University of California, San Diego, CA 92093

Author contributions: J.H., T.A.P., P.L., and Z.C. designed research; J.H., K.Y., J.W., S.W., and M.L. performed research; J.W., S.W., M.L., H.G., Z.H., Y.Y., K.K., A.L., and S.Y. contributed new reagents/analytic tools; J.H., K.Y., G.H., and A.U.M. analyzed data; and J.H., G.H., P.L., and Z.C. wrote the paper.

The authors declare no competing interest.

This article is a PNAS Direct Submission.

[1]To whom correspondence may be addressed. Email: jholo@stanford.edu, piliu@ucsd.edu, or zhc199@ucsd.edu.

This article contains supporting information online at https://www.pnas.org/lookup/suppl/doi:10.1073/pnas.2310714120/-/DCSupplemental.

Published October 2, 2023.

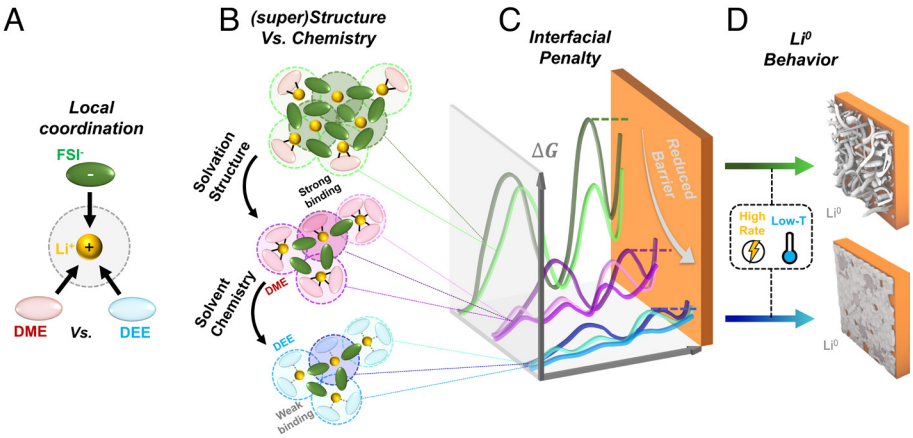

Fig. 1. Schematic overview of this work. The intertwined effects of (*A*) local and (*B*) long-range Li^+ solvation states and their influence on (*C*) desolvation kinetics at the interface and (*D*) Li metal cycling behavior under kinetic strain.

Within LMB electrolyte chemistries, a growing number of works, including those from our group, have demonstrated that the desolvation penalty at low temperature can be meaningfully improved through tailoring the Li^+ solvation structure (28–33). Early works in this area demonstrated that applying solvents that bind weakly with Li^+ in solution does so, where Li^+/anion coordination is observed in tandem with reduced charge-transfer impedance (28, 34). Computationally, we predicted that FSI^--bound Li^+ solvation structures found in diethyl ether (DEE) electrolytes approach the polarized interface in a more facile manner compared to solvent-coordinated structures, simplifying the desolvation process (30). Experimentally, we also observed inducing ion pairing in an electrolyte system applying 1, 2-dimethoxyethane (DME), a strongly bound solvent, lead to substantially improved low-temperature LMB performance (29). Hence, there is substantial evidence to suggest that both solvent chemistry *and* the local Li^+ solvation structure play a role in defining the desolvation resistance. However, a more quantitative description and control of the solvation structure is necessary for more precise control of the Li^+ behavior at the interface which dictates further advances in performance, particularly under low temperatures and high cycling rates.

As the identity and relative ratio between the solvent and salt define the solvation structure of conventional electrolytes, studies aimed at deconvoluting the effect of chemistry and structure are rare. Efforts to do so are further complicated by limitations in our understanding of solvation states at a quantitative level, where broad conclusions are generally made based on whether or not Li^+ is (semi)coordinated by the anion(s). Furthermore, while these bulk solvation descriptors are most often correlated to observed behavior, understanding how these descriptors contribute to the energetic landscape of the electrode/electrolyte interface remains a challenge. Such correlational analysis also betrays the inherent complexity of the interfacial Li^+ behavior which underlies desolvation and charge transfer. To make further progress in solvation-oriented electrolyte design, a more quantitative description of the Li^+ microstates present in a given electrolyte must be considered and causally connected to their desolvation behavior at the polarized interface.

To improve the understanding of these effects, we look toward localized-high-concentration electrolytes (LHCE) systems, which provide the opportunity to define local Li^+ solvation structure through tuning the molar ratio of constituents independent of the bulk solution viscosity (Fig. 1*A*). Tuning the local solvation structure in strongly and weakly bound solvents composed LHCE systems allows us to directly compare different solvent chemistries at fully optimized degrees of ion pairing. Crucially, we discover that the optimum degree of ion pairing in LHCE systems of interest is not at the saturation point and, instead, slight local dilution away from saturation greatly benefits the low-temperature and high-rate operation of the Li metal anode. This behavior was found to be a direct result of improved charge-transfer kinetics through distribution of relaxation times (DRT) analysis. Further, through accelerated molecular dynamics (MD) analysis, we predict that this optimized behavior is a direct result of distinct partially solvent-coordinated states that are emphasized through the introduction of local dilution to each system (Fig. 1 *B* and *C*). The effects of simultaneous optimization of LHCE chemistry and structure are then demonstrated in lab-scale and practical LMB full cells under fast-charging and low-temperature cycling (Fig. 1*D*). These results prompt the need for a more sophisticated view of Li^+ solvation in next-generation LMB electrolytes, where special attention should be paid to the speciation of quantitative solvation states to achieve state-of-the-art performance.

Results and Discussion

In this work, we primarily compare the properties and electrochemical performance of LHCE systems composed of lithium bis(fluorosulfonyl)imide (LiFSI), bis (2,2,2-trifluoroethyl) ether (BTFE), and either DME or DEE as the solvating solvent. These two nonfluorinated ethers were selected both due to their well-established compatibility with the Li metal anode and their contrasting binding energies with Li^+ (28, 35–37). To support an investigation of the local structure at a potentially wide range of local concentrations, we have limited the solvents to the ether family due to their intrinsic reductive stability vs. Li metal, as opposed to other chemistries which rely on high local concentration for reversible behavior (24). As a representative example, the Li^+/single-solvent binding free energies were calculated to be –62.1 and –43.1 kcal mol^{-1} for DME and DEE, respectively, via density functional theory (DFT) (Fig. 2*A*). Note that "Localized DME" (LDME) and "Localized DEE" (LDEE) is used to note LHCEs based on DME and DEE (i.e., LiFSI–DME–BTFE and LiFSI–DEE–BTFE mixtures), respectively. Within these two solvating solvent systems, we first optimize for *global dilution* by tuning the BTFE composition. As BTFE does not meaningfully solvate Li^+, tuning its composition acts to effectively reduce the overall electrolyte viscosity and total salt concentration without altering local solvation (Fig. 2*A*) (24, 38). To determine the optimal global

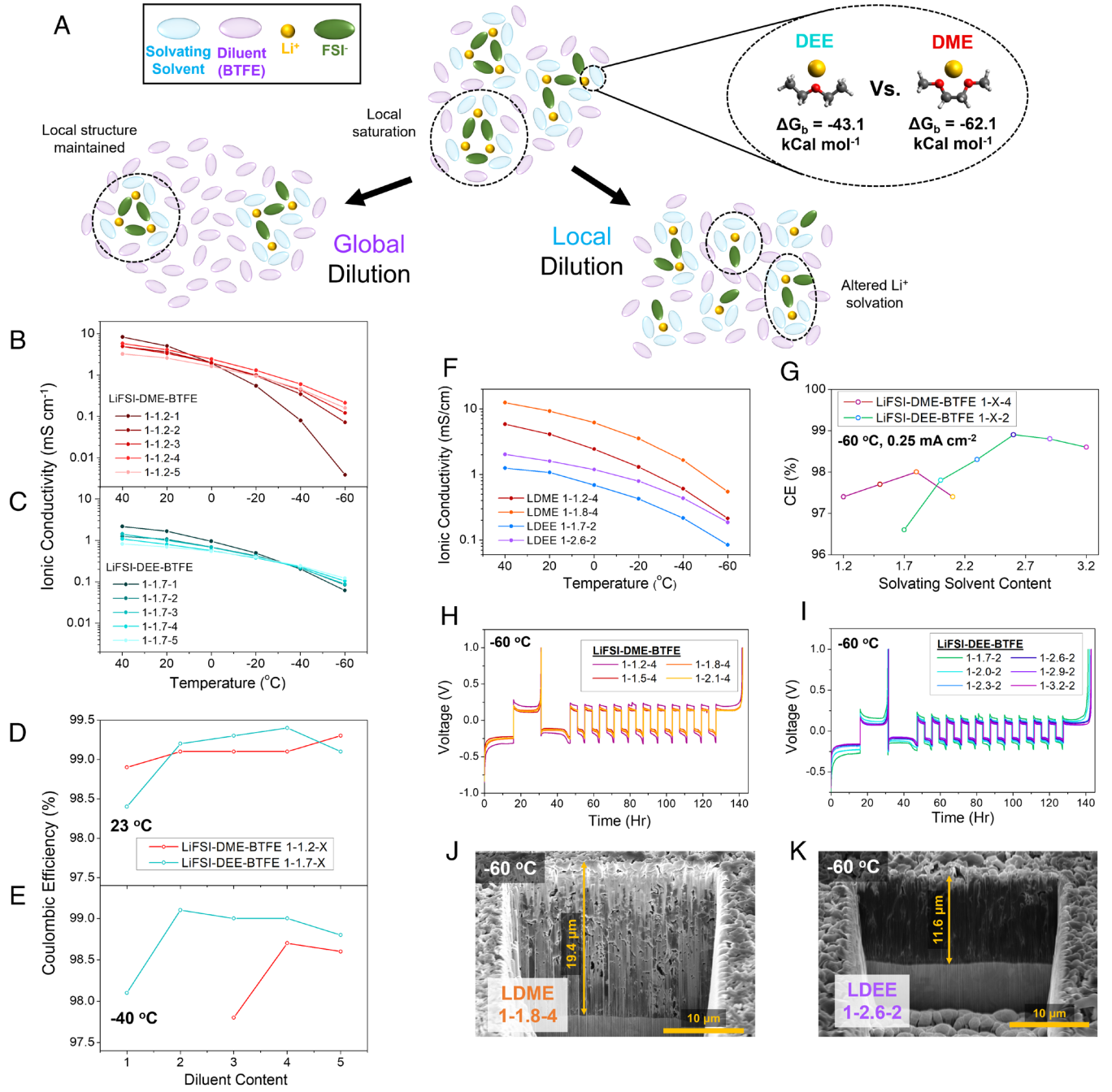

Fig. 2. Impact of LHCE dilution on Li metal anode performance. (*A*) Schematic overview of global and local dilution for LHCE systems composed of DEE (LDEE) and DME (LDME). Binding free energies for Li^+/DEE and Li^+/DME were calculated at the M06-HF//6-311++G** level of theory in DFT. Ionic conductivities of (*B*) LDME and (*C*) LDEE systems at ~saturated salt/solvating solvent ratio as a function of BTFE amount. Summary of Li||Cu CE measurements at 23 and −40 °C and 0.5 mA cm^{-2} in (*D*) LDME and (*E*) LDEE systems as a function of global dilution. (*F*) Ionic conductivities of LDME and LDEE systems at ~optimal BTFE amounts as a function of local dilution. (*G*) Summary measured Li CE for LDME and LDEE systems as a function of DME and DEE content at −60 °C and 0.25 mA cm^{-2}. Voltage curves of measurements in (*H*) LDME and (*I*) LDEE systems at 0.25 mA cm^{-2} as a function of local dilution. SEM microscopy of 1.8 mAh cm^{-2} Li metal plated at −60 °C and 0.25 mA cm^{-2} after cryo-FIB milling in (*J*) LDME 1.8, and (*K*) LDEE 2.6.

dilution of each system, we fix the LiFSI/solvating solvent ratio to their saturation points, which was found to be ~1:1.2 for DME and 1:1.7 for DEE. As shown in Fig. 2*B*, this global dilution has a significant effect on the ionic conductivity of the LDME system, where LDME 1-1.2-1 exhibits a maximum conductivity of 5.1 mS cm^{-1} at 20 °C yet decreases by three orders of magnitude (to 0.0039 mS cm^{-1}) at −60 °C. We believe this behavior to be a result of the increased viscosity, which is well known to overwhelm the low-temperature behavior of high-concentration solutions (31, 39). This low-temperature scaling behavior tends to improve as the BTFE content increases at the expense of ambient temperature conductivity, where the LDME 1-1.2-4 exhibits a reasonable balance of 4.1 and 0.21 mS cm^{-1} at 20 and −60 °C, respectively (Fig. 2*B*). LDEE systems, on the other hand, display a much weaker dependence on BTFE content, where LDEE 1-1.7-2 exhibits ionic conductivity of 1.07 and 0.085 mS cm^{-1} at 20 and −60 °C, respectively (Fig. 2*C*).

To better quantify the impact of global LHCE dilution on electrochemical behavior, we conduct Li metal CE testing using the accurate determination method in Li||Cu cells (40, 41). As

shown in *SI Appendix*, Fig. S1 *A* and *B*, both LDME and LDEE electrolyte systems are well suited for Li metal anode applications, displaying cycling overpotentials <30 mV and reversibility characteristic of LHCE systems based on LiFSI. Excluding LDEE 1-1.7-1, we find that all measured CE values exceed 99% at 23 °C and 0.5 mA cm^{-2} (Fig. 2*D*). The cycled Li morphology between LDME 1-1.2-4 and DEE 1-1.7-2 both appear to show a dendrite-free morphology with deposits on the range of 5 to 10 μm and plated thicknesses of 8.6 and 9.4 μm as observed via scanning electron microscopy (SEM) (*SI Appendix*, Fig. S2). The SEI formed in each electrolyte was also found to be nearly identical both in detailed composition and atomic composition across etching depth as observed in x-ray photoelectron spectroscopy (XPS) (*SI Appendix*, Fig. S3).

Despite their similar room-temperature performance, we find that the LDME 1-1.2-1 and 1-1.2-2 systems fail to cycle at −40 °C, likely as a result of the aforementioned increased viscosity (*SI Appendix*, Fig. S1*C*). Among the cyclable LDME systems, however, we find a peak CE of 98.7% for the 1-1.2.4 electrolyte, which confirms the advantageous behavior observed in the ionic conductivity measurements (Fig. 2*E*). The LDEE electrolytes, on the other hand, were all found to cycle reversibly at −40 °C, with a peak CE of 99.1% for the LDEE 1-1.7-2 system (*SI Appendix*, Fig. S1*D* and Fig. 2*E*). We also note the choice of diluent has a substantial effect on the ion transport and Li metal performance. As shown in *SI Appendix*, Fig. S4, when BTFE is replaced with the commonly applied 1,1,2,2-tetrafluoroethyl-2,2,3,3-tetrafluoropropyl ether, the temperature dependence of the LDEE's ionic conductivity is exacerbated, and the overpotential of Li cycling is substantially increased at −40 °C. For the sake of further system examination and optimization, we opt to fix the BTFE content at their optimum values of 4 for LDME and 2 for LDEE for the remainder of this work.

Recent works have signaled the importance of "weak" solvation effects in stabilizing the reversibility Li metal anode at low temperatures (28, 31, 42–44). In these electrolytes, reduced enthalpic binding energy between Li^+ and the solvent induces ion pairing between Li^+ and FSI^-, resulting in the formation of "contact ion pair" (CIP) solvation structures in which Li^+ is coordinated by solvent and exactly 1 FSI^- and "aggregate" (AGG) solvation structures in which Li^+ is coordinated by 2 or more FSI^-, to the point where the solvent can be completely displaced from a given shell (29, 30, 45, 46). Some research has even endeavored to further distinguish between specific AGG motif, for example, "AGG-I", "AGG-II", etc (45). While ion-paired structures have been proposed to be beneficial in reducing the desolvation barrier, the wide range of possible ion-paired states prompts inquiry into whether certain states would yield beneficial kinetic performance over others. To continue improving the performance of the Li metal anode under kinetic strain, it follows that identifying an optimal degree of local ion pairing in the electrolyte would be potentially beneficial.

To do so, we explore the impact of "local dilution" by tuning the composition of either DME or DEE in LHCE systems with fixed (~optimized) BTFE content (Fig. 2*A*). Specifically, we slightly dilute the saturated LDME and LDEE systems between 1.2 and 2.1 and 1.7 and 3.2 mol fractions, respectively, so as to alter local solvation (e.g., degree of ion pairing) with minimal impact on bulk solution properties. At −40 °C, we observe very little difference in measured Li||Cu CE, where LDME and LDEE systems retain efficiencies around 98% and 99%, respectively, regardless of local dilution (*SI Appendix*, Fig. S5 *A*–*C*). Similarly, we observe that the LDME 1-1.8-4 and LDEE 1-2.6-2 electrolytes produce nearly identical Li cycling CE at room temperature (*SI Appendix*, Fig. S4*D*). Unsurprisingly, this comparable room-temperature performance is supported by similar Li deposition morphology observed via SEM (*SI Appendix*, Fig. S6) and SEI chemistries across etching depths via XPS (*SI Appendix*, Fig. S7).

When cycled at −60 °C, however, the systems were found to display an acute dependence on solvating solvent content. As shown in Fig. 2*G*, we observe that the locally saturated LDME 1-1.2-4 and LDEE 1-1.7-2 struggle to retain high measured CE, exhibiting only 97.4 and 96.6% respectively. However, local dilution via the aforementioned addition of solvating solvent significantly improved CE, where LDME 1-1.8-4 and LDEE 1-2.6-2 systems displayed peak CEs of 98.0 and 98.9%, respectively. In addition to the beneficial effect of local dilution on ultralow temperature Li cycling, we also note that the LDEE optimum CE significantly exceeds the LDME optimum CE. Moreover, via cryogenic focused ion beam (cryo-FIB) milling integrated SEM, we find that the plated Li produced by LDEE 1-2.6-2 is substantially less porous than that plated in LDME 1-1.8-4, showing thicknesses of 11.6 and 19.4 μm, respectively, for 1.8 mAh cm^{-2} Li (Fig. 2 *J* and *K*). This trend is also true of Li plated at −40 °C, where LDEE 1-2.6-2 and LDME 1-1.8-4 systems produce Li thicknesses of 10.4 and 16.5 μm for 1.8 mAh cm^{-2} Li, respectively (*SI Appendix*, Fig. S8). This behavior indicates that once an optimum degree of ion pairing has been reached in each respective system, the weakened binding of DEE still plays an important role in improved performance.

It is also important to note that this local dilution has a beneficial impact on the ionic conductivity of LDEE and LDME solutions, where each experiences a meaningful upshift across 40 to −60 °C (Fig. 2*F*). This effect has been observed in our previous work and, while meaningful, does not fully account for the improvement in low-temperature CE. First, despite the relative improvements between LDEE 1-1.7-2 and LDEE 1-2.6-2, both solutions produce lower ionic conductivities than both LDME 1-1.2-4 and LDME 1-1.8-4 electrolytes. Further, the −60 °C CE optima "peak" exists at 1.8 for LDME and 2.6 for LDEE, instead of continuing to increase monotonically as solvating solvent content, and ionic conductivity, increases. Similarly, Li plated cycled −60 °C shows a somewhat similar SEI between LDME 1-1.8-4 and LDEE 1-2.6-2 (*SI Appendix*, Fig. S9). Although SEI variance can be observed for a given LHCE system as a function of local dilution (*SI Appendix*, Figs. S3 and S7) or as a function of cycling temperature (*SI Appendix*, Figs. S7 and S9), these variations do not explain the differences in low-temperature CE's between LDEE and LDME systems of comparable local dilution. These factors, in addition to the growing body of literature which argues for desolvation-defined low-temperature behavior indicate that neither ion transport nor SEI chemistry improvements produce the aforementioned CE variance across LCHE systems (12, 14, 26, 43). Hence, we conclude that reduced solvent binding (LDEE vs. LDME) and optimal local structure (degree of local dilution) yield improved desolvation-related charge-transfer kinetics.

In addition to the low-temperature performance, we find that the combination of weak solvent binding and local dilution supports high-rate Li metal cycling. In Li||Cu cells applying the locally saturated and locally optimized LDME and LDEE, we employ a variable rate cycling staircase from 0.5 to 10 mA cm^{-2} with a fixed plating capacity of 1 mAh cm^{-2} (Fig. 3*A*). Under this protocol, we observe that the LDEE systems significantly outperform the LDME systems at high rates despite comparable low-rate CE. Specifically, the LDEE electrolytes retain CE values of >97% at 10 mA cm^{-2} where the LDME systems rapidly decay to <90%. Additionally, it is observed that the LDEE 1-2.6-2 system produces slightly higher CE than LDEE 1-1.7-2 at each respective cycling rate. As this short-term staircase protocol does not allow sufficient conditioning

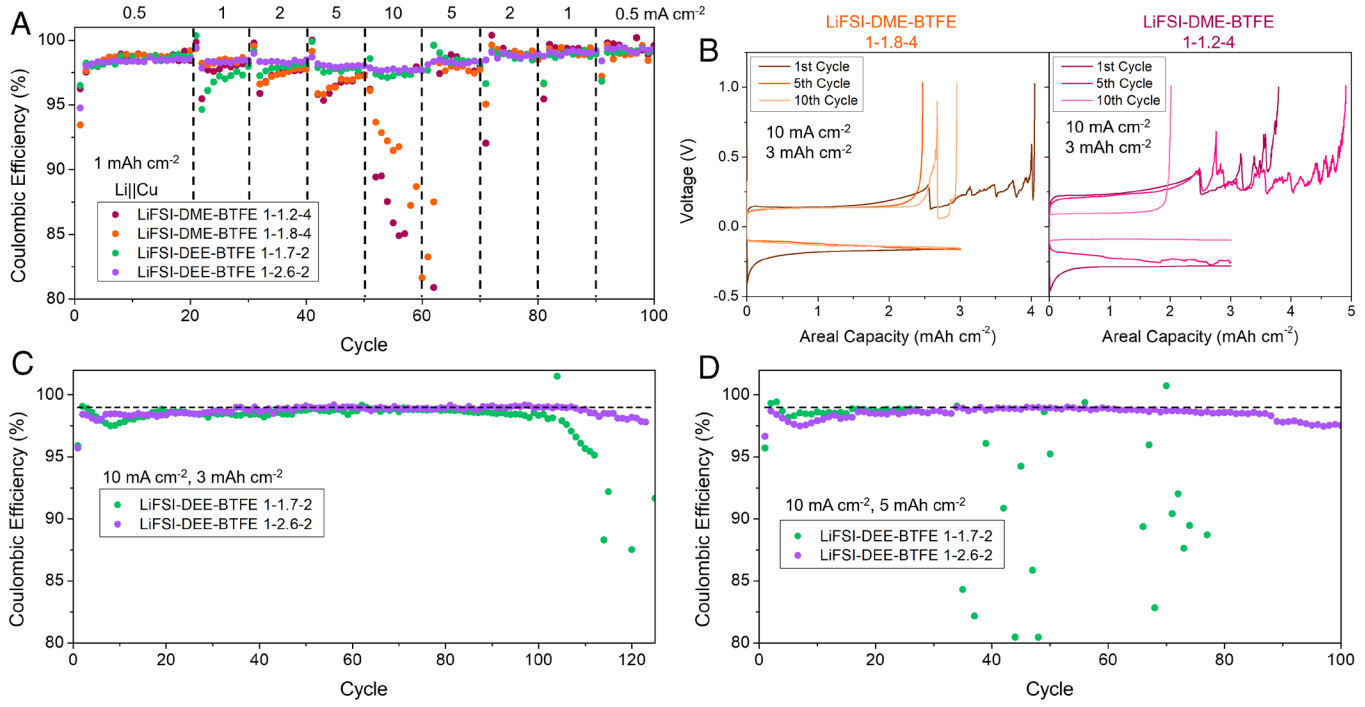

Fig. 3. High-rate performance of Li||Cu cells in the LHCE systems of interest. (*A*) Variable rate CE of Li||Cu cells employing LHCE systems of interest. (*B*) Voltage profiles of Li||Cu cells employing LDME electrolytes operated at 10 mA cm^{-2} and 3 mAh cm^{-2}, where shorting was observed in both cases. (*C*) CE of Li||Cu cells employing LDEE electrolytes at 10 mA cm^{-2} and 3 mAh cm^{-2}. (*D*) CE of Li||Cu cells employing LDEE electrolytes at 10 mA cm^{-2} and 5 mAh cm^{-2}. The horizontal dashed lines in (*C*) and (*D*) are at 99%.

and stabilization at each rate of interest, we also conduct long-term cycling at 10 mA cm^{-2} and 3 mAh cm^{-2}, a capacity more representative of practical cathode loadings. Under this protocol, we find that cells containing both LDME electrolytes short in the first cycle, which persists in following cycles (Fig. 3*B*). The LDEE electrolytes, on the other hand, provide up to 100 cycles of stable performance, with CEs approaching 99% after ~30 cycles (Fig. 3*C*). Again, it is observed that the LDEE 1-2.6-2 electrolyte maintains a slightly higher CE and ~20 more stable cycles than its locally saturated counterpart. This difference is further emphasized when the plated capacity is increased from 3 to 5 mAh cm^{-2}, where the LDEE 1-2.6-2 electrolyte produces up to 100 cycles and approaches 99% CE after 30 conditioning cycles, whereas the LDEE 1-1.7-2 cell begins shorting after only 28 cycles (Fig. 3*D*). Given the ambient temperature condition, this improvement could be attributed to the improved ionic transport; however, the superiority of LDEE over LDME indicates that charge-transfer effects are still an important consideration.

To characterize such charge-transfer effects, we take inspiration from Li et al., who demonstrated the decoupling of SEI and desolvation-related limitations through a precycling method (14). We slightly modify their workflow, first cycling a Li||Li cell in a given LHCE system (E1 in Fig. 4*A*) to build up an SEI derived from E1, as well as to increase the electrochemically active surface area (ECSA) and minimize contributions from nucleation. Afterward, we disassemble said Li||Li cell and reassemble a separate cell with the precycled Li electrodes with either the same electrolyte as that which was used during precycling (E1) or a separate one (E2). These newly assembled cells are subjected to electrochemical impedance spectroscopy (EIS) at various temperatures of interest (Fig. 4*A*). Implementation of EIS as opposed to other voltametric analyses for Li metal is critical, as the low current passed limits any significant change in ECSA during the measurement. Accordingly, we primarily consider the change in relative impedance as a function of temperature to eliminate the influence of initial ECSA in the samples from precycling. These data are then fit via the DRT model, in which the cell impedance is fit as a continuum of repeating parallel RC circuits and allows for kinetic analysis of the cell as a function of time constant (Fig. 4 *A*, *Bottom*) (47). Assuming the E1-derived SEI is maintained during reassembly and EIS does not meaningfully change said SEI, which is reasonable given the similar electrolyte chemistries and measured CE values and the low current passed during EIS, this technique allows us to decouple SEI and desolvation limitations for low-temperature Li metal operation.

First, we apply this analysis to observe variance between the optimized LDME 1-1.8-4 and LDEE 1-2.6-2 (shown as LDME 1.8 and LDEE 2.6 in Fig. 4) systems. The DRT fits produced from raw EIS data in *SI Appendix*, Fig. S10 are shown in Fig. 4*B*, where two peaks are generally observed, representing two distinct time relaxation regimes, regardless of temperature. It is widely reported that the higher time constant peak is associated with charge transfer due to its coupling with the double-layer capacitance (27, 47). To directly observe differences in temperature dependence between electrolyte systems without the influence of differences in cycled surface area and cell-to-cell variance, we consider a relative impedance normalized to the charge-transfer peak maxima at room temperature. When comparing LDME 1-1.8-4 and LDEE 1-2.6-2, it is immediately clear that despite competition at room-temperature, the charge-transfer impedance rapidly outpaces SEI as the temperature is decreased (Fig. 4 *C* and *D*). Moreover, we find that said dominating charge-transfer peak is largely defined by the electrolyte injected after precycling.

We also conduct a similar analysis to probe the effects of local dilution among the same solvating solvent, where the same precycling and reassembly procedure is applied to combinations of LDME 1-1.2-4 // LDME 1-1.8-4 and LDEE 1-1.7-2 // LDEE 1-2.6-2 (*SI Appendix*, Figs. S10 and S11). This analysis reveals a similar phenomenon, where the electrolyte present during the EIS measurement primarily determines the charge-transfer-dominated

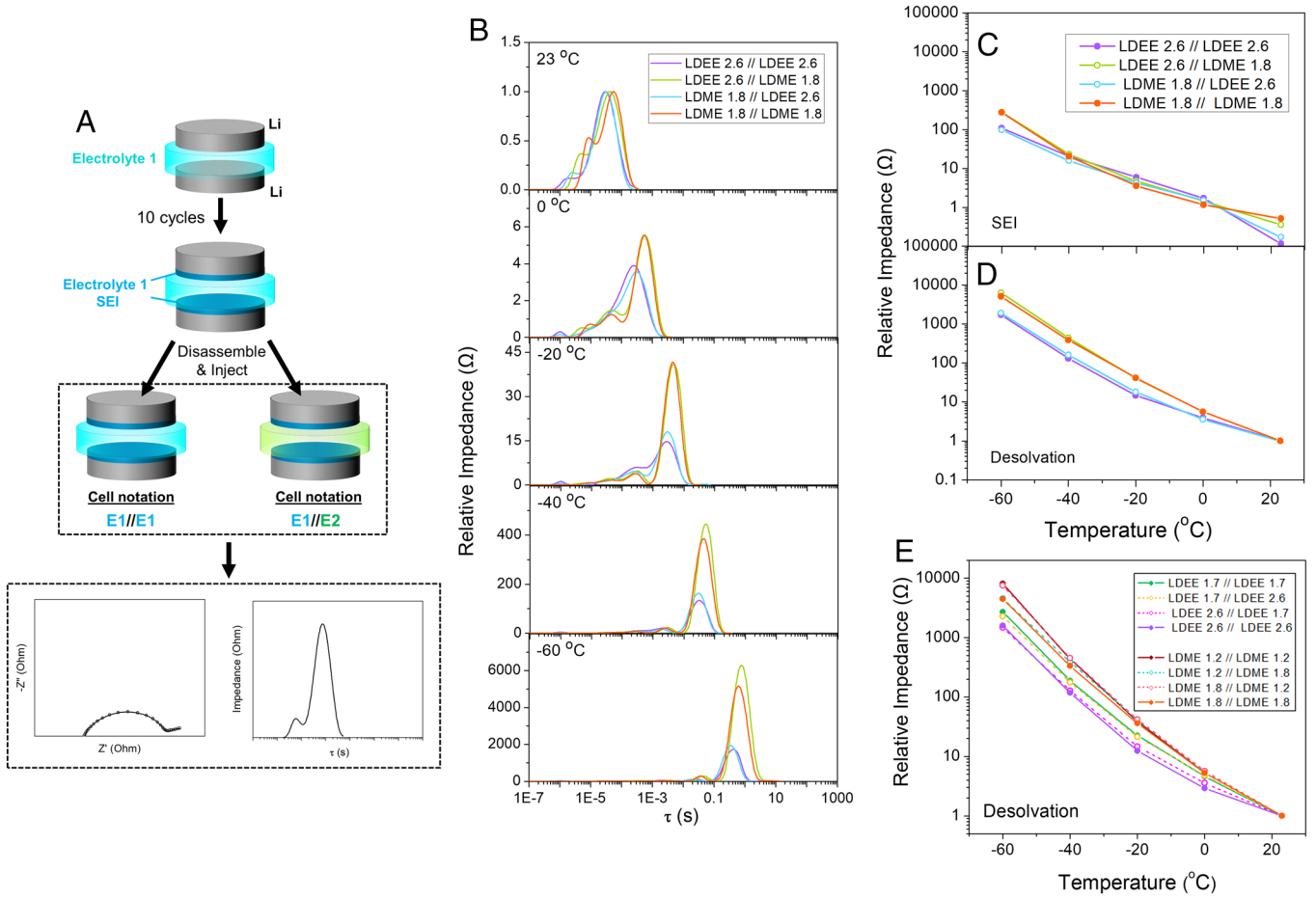

Fig. 4. Impedance-based analysis of Li metal in electrolytes of interest. (*A*) Schematic of cell preparation technique. (*B*) DRT profiles from EIS measurements between 23 and −60 °C. Impedance values for each system are normalized to their charge-transfer peak maxima measured at room temperature. Summary of peak maxima as a function of temperature in the LDME 1.8 and LDEE 2.6 electrolyte testing matrix for (*C*) SEI and (*D*) charge transfer peaks. (*E*) Summary of charge-transfer peak maxima as a function of temperature in the LDEE and LDME dilution testing matrices. Note that the values following LDEE and LDME denote solvating solvent content, where all LDEE systems follow compositions of 1-X-2 and LDME systems follow compositions of 1-X-4. In all cases, DRT fitting after the semicircle was neglected due to Warburg incompatibility with the technique.

impedance limitations at low temperature (Fig. 4*E*). It is also noteworthy that the LDEE 1-1.7-2 electrolyte (regardless of SEI) displays a weaker overall temperature dependance than the LDME systems, which implies that its reduced ionic conductivity likely contributes to its low CE at −60 °C. We note that these observations are likely specific to largely inorganic SEI compositions and may break down in the context of semiorganic SEIs, where polymeric species would effectively solvate Li^+ at the interface (48, 49). Along these lines, we find that the addition of 5% (v/v) of fluoroethylene carbonate (FEC) to the LDEE 1-2.6-2 electrolyte substantially reduces CE to only 96.4% and increases observed overpotential at −60 °C (*SI Appendix*, Fig. S12). These data confirm that the variations in low-temperature performance related to solvent chemistry and local dilution are associated with desolvation-dominated charge transfer, where the small differences between SEIs generated in the LHCE systems are of little consequence.

To gain a molecular understanding of the effect of local dilution in LDME and LDEE electrolytes on the Li^+ desolvation process at the electrified interface, we apply a metadynamics (MTD) approach developed in our previous work (see experimental and computational methods) (30). Implemented through accelerated classical MD simulations employing traditional forcefields, this approach allows us to resolve free-energy spectra of Li^+ in an electrolyte phase space described by multidimensional collective variables beyond what is thermally accessible in conventional MD (50–53). First, we examine the equilibrium structure of Li^+ in LDME 1-1.2-4, LDME 1-1.8-4, LDEE 1-1.7-2, and LDEE 1-2.6-2 in the bulk (Materials and Methods) with a representative cell snapshot shown in Fig. 5*A*. After MD equilibration, the average solvation structures of LDME 1-1.2-4 and LDME 1-1.8-4 were found to be $Li^+(DME)_{0.96}(FSI^-)_{2.1}$ and $Li^+(DME)_{1.3}(FSI^-)_{1.6}$. For LDEE 1-1.7-2 and LDEE 1-2.6-2, a similar shift toward solvent coordination is observed via local dilution, with average solvation structures of $Li^+(DEE)_{0.8}(FSI^-)_{3.0}$ and $Li^+(DEE)_{1.2}(FSI^-)_{2.8}$ (*SI Appendix*, Fig. S13). It is important to note that structures with FSI^- coordination number (CN) > 1 are canonically described as ion AGG, which are a well-known feature of LHCE and weakly solvating electrolyte systems.

To go beyond an "average" solvation structure, and further differentiate between distinct solvation microstates, we apply 1-D MTD to resolve free-energy minima as a function of DME/DEE oxygen CN and total CN. As shown in Fig. 5*B*, the relative increase in DME coordination induced through local dilution is seen primarily as a shift in local minima away from the $Li^+(FSI^-)_4$ and $Li^+(DME)_1(FSI^-)_2$ states (obtained from total CN minima, *SI Appendix*, Fig. S14) in LDME 1-1.2-4 toward $Li^+(DME)_1(FSI^-)_2$ and $Li^+(DME)_2(FSI^-)_1$ in LDME 1-1.8-4. The latter of these two states is known as a CIP. In the LDEE case, this same shift toward DEE coordination is seen with local dilution, where the $Li^+(FSI^-)_4$

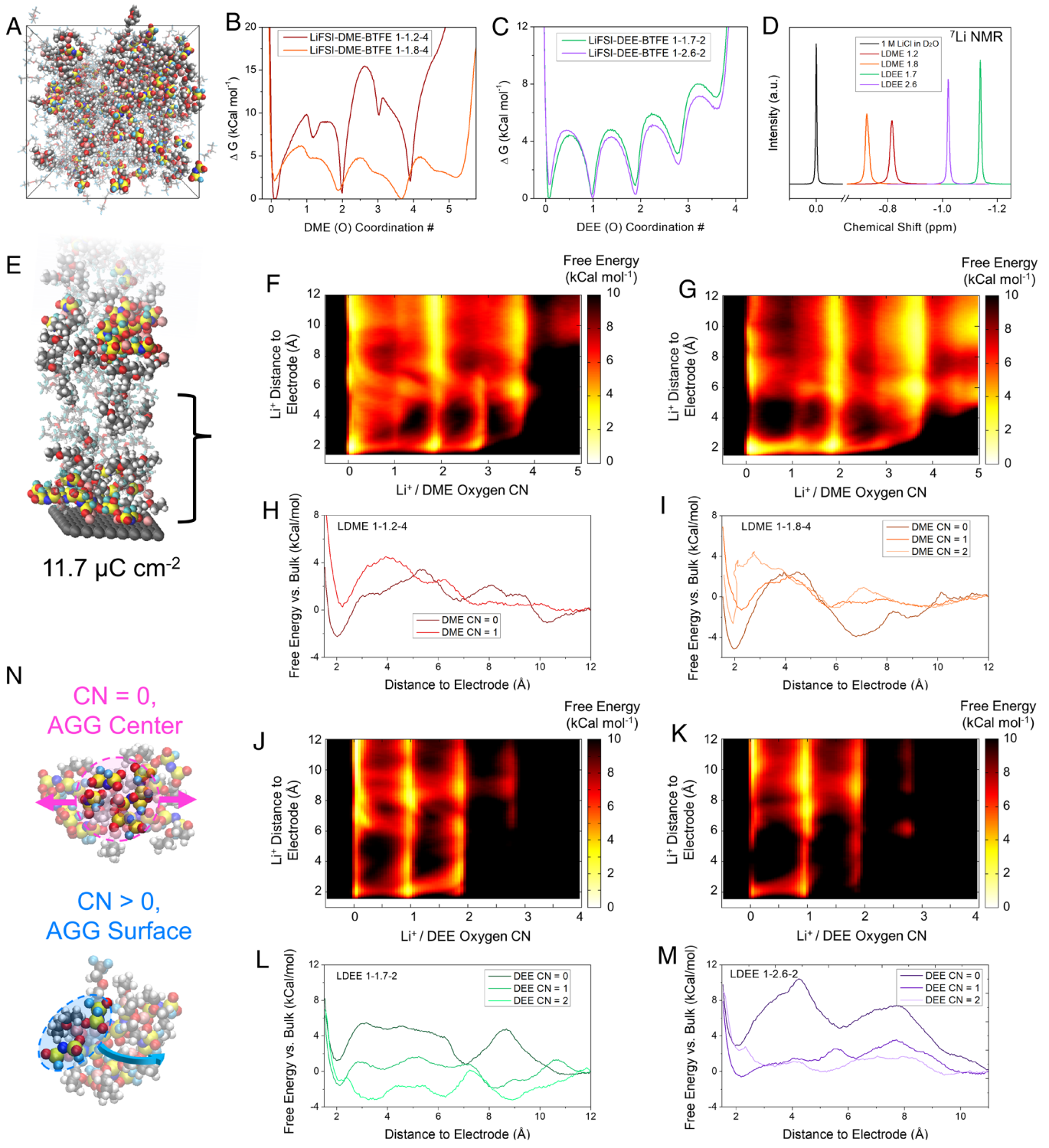

Fig. 5. Microscopic analysis of electrolyte structure and thermodynamics in the bulk and at an electrochemical interface. (*A*) Representative MD snapshot (LDME 1.8 shown here) of bulk electrolyte used in *B* and *C*. (*B*) 1-D free-energy profiles of LDME 1.2 and 1.8 with respect to DME O coordination (Note that DME contains 2 oxygen atoms per molecule). (*C*) 1-D free-energy profiles of LDEE 1.7 and 2.6 with respect to DEE O coordination. (*D*) Measured ^{7}Li (194 MHz) NMR spectra of LHCE systems relative to 1 M LiCl in D_2O. (*E*) Representative MD snapshot (LDME 1.8 shown here) of biased (11.6 to 11.7 μC cm^{-2}) interface simulations used in *F*–*M*. 2-D free-energy spectra of (*F*) LDME 1-1.2-4, and (*G*) LDME 1-1.8-4 at the electrochemical interface with respect to Li^+/electrode distance and Li^+ DME O coordination. 1-D free-energy pathways taken from 2-D spectra (*Materials and Methods*) for (*H*) LDME 1.2, and (*I*) LDME 1.8. 2-D free-energy spectra of (*J*) LDEE 1-1.7-2, and (*K*) LDEE 1-2.6-2 at the electrochemical interface with respect to Li^+/electrode distance and Li^+ DME O coordination. 1-D free-energy pathways taken from 2-D spectra (*Materials and Methods*) for (*L*) LDEE 1.7, and (*M*) LDEE 2.6. (*N*) Schematic of solvent CN-dependent Li^+ migration pathways at the interface.

and $Li^+(DEE)_1(FSI^-)_3$ and minima in LDEE 1-1.7-2 shift to $Li^+(DEE)_1(FSI^-)_3$ and $Li^+(DEE)_2(FSI^-)_3$ in LDEE 1-2.6-2 (Fig. 5*C*). As previously discussed, all of the studied LHCE systems display persistent ion aggregation. However, this variance in local preferred solvation state also generates substantial variance in the scale of said AGG complexes in solution. In this regard, local solvation states composed entirely of anion coordination [i.e., $Li^+(FSI^-)_4$] would only be found at the center of an AGG, whereas

partial solvent coordination and FSI^- CN > 1 would be found at an AGG surface site. This implies that LDME 1-1.2-4 and LDEE 1-1.7-2, which demonstrate a preference toward $Li^+(FSI^-)_4$ (i.e., lower AGG surface to volume ratio) would produce larger AGG structures. Indeed, 1-D MTD simulations with respect to Li^+ self-coordination confirm this to be the case (*SI Appendix*, Fig. S15), a fact that is visually apparent in MD simulation snapshots of the systems of interest (*SI Appendix*, Fig. S16).

To provide experimental evidence of these predictions, we also conduct ^{7}Li NMR on the solutions of interest (Fig. 5*D*). First, a substantial variance in the chemical shift of the ^{7}Li peak is observed between LDME and LDEE systems, which is a well-established feature of altered solvent chemistry, though the origin of this phenomena is largely unknown (54). However, within each solvent chemistry, we observe a significant upfield shift as a result of decreased ion pairing in solution, consistent with the results of our simulations (55, 56). These trends are also observed in the Raman spectra of the electrolytes of interest, where the S-N-S bending mode of FSI^- in LDME 1.8 and LDEE 2.6 electrolytes display shifts toward lower wavenumber, indicative of reduced ion pairing (*SI Appendix*, Fig. S17). We also conduct the same ^{7}Li NMR studies as a function of temperature, where we observe a distinct downfield shift for each system of ~−0.225 and ~−0.34 ppm for the LDME and LDEE systems, respectively, between 25 and −60 °C (*SI Appendix*, Fig. S18). As reduced temperatures have been hypothesized to incentivize solvent coordination, we hypothesize that this shift is due to a constriction of the solvation shell, increasing the local electron density around the Li^+ in solution (30, 57, 58).

To understand the impact of the local-dilution-driven solvation shifts on the behavior of Li^+ at the electrified interface, we conduct MD and MTD simulations of LHCE systems in contact with a negatively charged (11.7 μC cm^{-2}) graphene electrode (Fig. 5*E*). This approach has been applied in previous works and provides an opportunity to study the ion desolvation process in the absence of a passivating interface by applying a negatively polarized electrode to supplant coordinating solvent and anions (*Materials and Methods*) (30, 52). As shown in *SI Appendix*, Fig. S19, the implementation of the model electrode drives specific adsorption of Li^+ and the simultaneous attraction of additional FSI^- in the EDL, implying that AGG structures are further stabilized at the interface. To accurately describe the phase-space of Li^+ at this interface, we conduct 2-D MTD with respect to both Li^+ position relative to the electrode (i.e., Li^+/electrode distance), and Li^+/solvating solvent CN (Fig. 5 *F*, *G*, *J*, and *K*). Generally, we observe that the shift toward solvent coordination via local dilution is also maintained in the EDL, further supporting the hypothesis that bulk solvation states persist at the electrochemical interface. However, a slight increase in total CN to ~5 in all systems (LDME 1.2 and LDEE 1.7 were previously ~4) is also observed (*SI Appendix*, Fig. S20), likely due to solution densification at the solid/liquid interface (*SI Appendix*, Fig. S19). As seen in the 2-D profiles, the solvent CN of each state in the bulk (>10 Å) is largely maintained as Li^+ undergoes desolvation, indicating that FSI^- is removed in the process, possibly assisted by coulombic repulsion from the negatively polarized electrode or adjacent anions (Fig. 5 *F*, *G*, *J*, and *K* and *SI Appendix*, Fig. S18).

To resolve the desolvation pathway for each solvation state, we sample 1-D "slices" of these 2-D profiles (Fig. 5 *H*, *I*, *L*, and *M*). These profiles are taken parallel to the *y* axis centered along the EDL minima for all states except for the DME Oxygen CN = 4 state in LDME 1-1.8-4, in which a rudimentary pathfinding script was applied (*Materials and Methods* and *SI Appendix*, Fig. S21). As the free energy of the 2-D profiles is relative to the phase-space minima, these profiles cannot be directly applied to derive electrochemical kinetic information. Instead, we normalize these profiles to their respective bulk free energy, arbitrarily defined as the maximum z distance of their sampling range, in order to make conclusions about their desolvation barriers relative to one another. In all LHCE systems, we observe that the solvent CN = 0, $Li^+(FSI^-)_5$ state experiences a heightened desolvation barrier relative to their neighboring partially solvent-coordinated AGG states (Fig. 5 *H*, *I*, *L*, and *M*). Considering the aforementioned spatial implications of the purely anion-coordinated state, we conclude that Li^+ preferentially moves along the surface of AGG superstructures at the electrochemical interface (Fig. 5*N*). The existence of these desolvation pathway does not correlate to an absolute AGG size (*SI Appendix*, Fig. S15) and instead depend on a relative size reduction away from the saturation point. These data imply that ostensibly minor variations in the relative solvation structure within a given electrolyte system can play a consequential role in the desolvation penalty at the interface.

Having determined the microscopic mechanisms for ion desolvation, we now provide a practical demonstration of the designed LHCE systems on Li metal full batteries at ultralow temperatures. We assemble full cells based on a 10 mg cm^{-2} $LiNi_{0.8}Co_{0.15}Al_{0.05}O_2$ (NCA) cathode and 20 μm Li anode (N/P ~ 2.3), with initial testing conducted in coin cells with flooded electrolyte (Fig. 6*A*). To confirm the baseline compatibility of the LHCE systems of interest with the full cell chemistry, we first conducted C/3 charge || C/3 discharge cycling at room temperature (Fig. 6*B*). Under these conditions, all cells were observed to show minimal capacity fade over 100 cycles, confirming a viable performance floor for later comparison under kinetically strained conditions. To confirm the trends observed in high-rate and low-temperature Li||Cu cells, we apply the coin-type full cells to fast-charging and low-temperature cycling. As shown in Fig. 6*C*, when cycled at 23 °C and a 20-min CC-CV (*Materials and Methods*) charging || C/3 discharging protocol, we find that the LDME 1-1.8-4, LDEE 1-1.7-2, and LDEE 1-2.6-2 electrolytes retain ≥125 mAh g^{-1} compared to only 105 mAh g^{-1} in LDME 1-1.2-4. Similar to the trends observed in Fig. 3, the inherently superior transport of the LDME electrolytes is not reflected in the cycling trends. Although ambient temperature behavior is not dominated by desolvation limitations as is the case in subzero conditions, this nonetheless implies a significant contribution from desolvation.

Next, we apply the optimized LDME 1-1.8-4 and LDEE 1-2.6-2 electrolytes in full cells cycling at reduced temperatures. As demonstrated in our previous work, the reduced parasitic reactivity offered by low temperatures provides the opportunity to increase the cutoff voltage of full cell cycling without meaningful reductions in cycle life (29). In this work, we find that applying cutoffs of 4.4 V at −40 °C and 4.5 V at −60 °C at C/10 charge || C/5 discharge rates are similarly viable (*SI Appendix*, Fig. S22). Under these conditions, we find that both the LDME 1-1.8-4 and the LDEE 1-2.6-2 electrolytes produce stable capacity retention at −40 °C, where the latter produces a slightly higher capacity of 137 mAh g^{-1} compared to 127 mAh g^{-1} (Fig. 6*D*). However, at −60 °C, we find that the difference in performance is enhanced, where the full cell employing the LDEE 1-2.6-2 electrolyte exhibits an initial reversible capacity of 108 mAh g^{-1} and 93% capacity retention over 100 cycles, compared to only 59 mAh g^{-1} and 15% in LDME 1-1.8-4 (Fig. 6*E*).

Lastly, to provide a demonstration of potential scalability for low-temperature LMBs employing locally optimized LHCE electrolytes, we assembled a single-layer 10 mg cm^{-2} NCA || 20 μm Li pouch cell with a lean-electrolyte loading of 3 g Ah^{-1} LDEE 1-2.6-2 (Fig. 6*F*). We then subjected this cell to variable-temperature

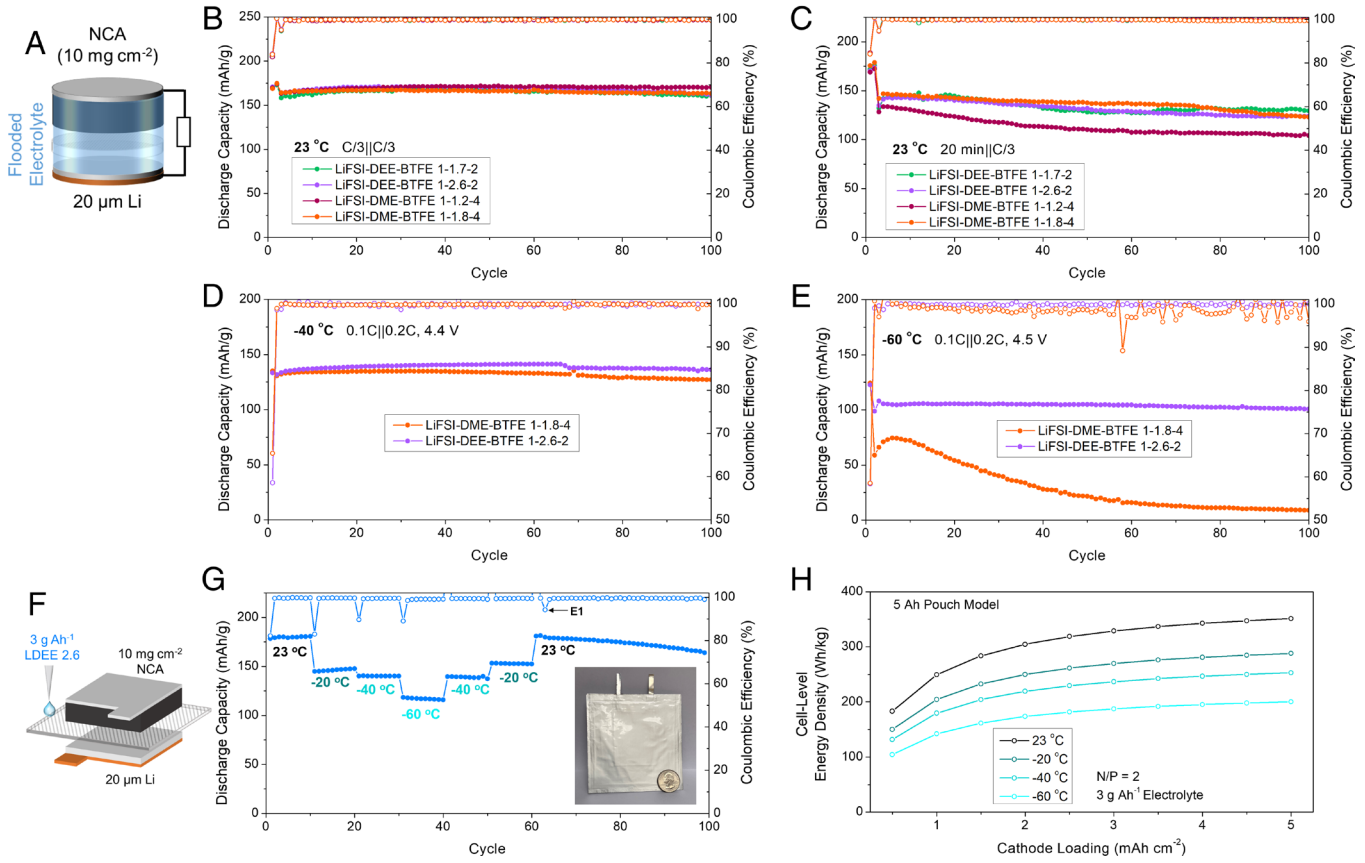

Fig. 6. Cycling behavior of Li metal full cells under reduced temperature of elevated charging rate. (*A*) Schematic of 20 μm Li || 10 mg cm^{-2} NCA coin-type full cells applied in (*B–E*). Cycling performance of cells at (*B*) 23 °C, C/3 charge || C/3 discharge and 4.3 V cutoff, (*C*) 23 °C, 20 min charge || C/3 discharge and 4.3 V cutoff, (*D*) −40 °C, C/10 charge || C/5 discharge and 4.4 V cutoff, (*E*) −60 °C, C/10 charge || C/5 discharge and 4.5 V cutoff. Cells in (*D* and *E*) are subjected to a single charge to 4.3 V at room-temperature before transferring to low-temperature. (*F*) Schematic and photo of single-layer 20 μm Li || 10 mg cm^{-2} NCA pouch-type full cells with 3 g Ah^{-1} LDEE 2.6 electrolyte. (*G*) Variable-temperature cycling of pouch-cell with 23 °C cycling at C/5 || C/3 and 4.3 V cutoff, −20 °C cycling at C/10 || C/5 and 4.3 V cutoff, −40 °C cycling at C/10 || C/5 and 4.4 V cutoff, and −60 °C cycling at C/20 || C/10 and 4.5 V cutoff. All cells use CC-CV charging with C/20 cutoff except for *C*, where the charge period is capped at 20 min, and *G*, where the low-temperature CV charge is capped at C/50. E1 refers to a cycler event in which the computer operating the battery cycler crashed and was not operating for ~3 d. (*H*) Cell-level energy density projections as a function of cathode loading and operating temperature (*Materials and Methods*).

cycling from room temperature to −60 °C (Fig. 6*G*). We find that the cell was able to perform with exceptional reversibility, where minimal capacity fade is observed at any of the ultralow temperature settings. Additionally, the cell is able to produce capacity retentions of 85.1, 77.6, and 65.4 % at −20, −40, and −60 °C, respectively (*SI Appendix*, Fig. S23). Additionally, we find that after returning the cell to 23 °C, the entirety of the initial room-temperature capacity is retained, and 164 mAh g^{-1} (93%) retention is produced after 100 total cycles (including low-temperature protocol). Although this demonstrated pouch cell is constrained to only a single layer, we believe that the demonstration of viable performance retention during low-temperature cycling under lean electrolyte conditions is a significant advance for the scalability of such systems.

To further understand the impacts of increasing the number of electrode layers, we apply a pouch cell energy density projection model which was modified based on the 18650 model published by Betz et al. and applied in our previous work (29, 59, 60). As shown in *SI Appendix*, Fig. S24, the projected cell-level energy density of the cell rapidly increases as the number of layers increases (i.e., the total cell capacity), where the conditions applied in our single-layer pouch would produce a ~300 Wh kg^{-1} cell at 50 layers. This value would exceed 350 Wh kg^{-1} at an increased cathode loading of 5 mAh cm^{-2}. Assuming a 5 Ah total pouch capacity, an N/P ratio of 2, 3 g Ah^{-1} electrolyte, and low-temperature energy retentions calculated in *SI Appendix*, Fig. S23, we project energy densities of 305, 250, 219, and 174 Wh kg^{-1} at 23, −20, −40, and −60 °C for a cathode loading of 2 mAh cm^{-2} (Fig. 6*H*). These values would similarly increase to 343, 281, 246, and 195 Wh kg^{-1} at the increased cathode loading of 4 mAh cm^{-2}. Keeping the long-term goals of LMB cell development in mind, we also predict that cell-level energy densities of 447, 367, 322, and 255 Wh kg^{-1} could be achieved at 23, −20, −40, and −60 °C if the cathode capacity could be increased to 220 mAh g^{-1}, cathode loading to 4 mAh cm^{-2}, and the electrolyte loading decreased to 2 g Ah^{-1} while maintaining the low-temperature performance retention demonstrated in this work (*SI Appendix*, Fig. S25).

Conclusion

Through the independent modulation of global dilution, local dilution, and solvent chemistry in LHCE systems composed of DME and DEE, we find that both the solvent binding and degree of ion pairing play critical roles in Li^+ desolvation kinetics. Crucially, we find that an optimum distribution of solvation states exists at a level of ion pairing less than the salt saturation limit of each system. These effects play a noteworthy role in improving the of the Li metal anode under kinetic strain, where slight local dilution produces measured CEs of 98.9 and 98.0% at −60 °C for LDEE and LDME systems, respectively. We also find that

implementation of DEE and local dilution facilitates the operation of Li metal anodes at 10 mA, 5 mAh cm^{-2} cycling conditions, where LDME cells short. These local dilution and solvent chemistry effects, which define low-temperature performance and significantly influence room-temperature reversibility at high rate, are a fundamental result of enhanced desolvation kinetics, which was deconvoluted through a DRT-based multisystem analysis. Through computational investigations, we predict that distinct solvation microstates, e.g., $Li^+(Solvent)_x(FSI^-)_y$, produce consequentially distinct desolvation barriers at the interface, where structures possessing low, nonzero amounts of coordinating solvent show superior kinetics. In this regard, local dilution further incentivizes the prevalence of such states, reducing long-range ion AGG size and facilitating facile Li^+ desolvation. These effects are then leveraged in NCA-based LMB full batteries, which show exceptional reversibility down to −60 °C and room temperature, 20-min fast-charging conditions. Such kinetically strained operation was also demonstrated in single-layer pouch cells under lean electrolyte loading, demonstrative of scaling potential. This work aims to demonstrate a more nuanced approach to solvation structure design in Li electrolytes, where controlling the distribution of individual microstates at the interface produces next-generation performance under kinetically strained operating conditions.

Materials and Methods

Materials. Anhydrous DME and DEE were purchased from Millipore-Sigma. Bis (2,2,2-trifluoroethyl) ether (BTFE) was purchased from Synquest. All solvents were dried with >10% (by weight) activated molecular sieves for at least 24 h before use. Lithium bis(fluorosulfonyl)imide (LiFSI) was obtained from Gotion and used as received. The electrolytes were prepared dissolving predetermined amounts of LiFSI salt into the solvents of interest with stirring. $LiNi_{0.8}Co_{0.15}Al_{0.05}O_2$ (NCA) cathodes were acquired from the Cell Analysis, Modeling, and Prototyping Facility at Argonne National Laboratory and are composed of 86:6:8 Toda NCA, conductive carbon, and poly(vinylidene difluoride) binder by weight. The loadings of these cathodes are 10 mg cm^{-2} NCA (~1.8 mAh cm^{-2}). All cells used a 25-μm Celgard 2,325 membrane. Li||Cu cells used 250 μm Li metal chips purchased from Xiamen TOB New Energy Technology Co. LTD. NCA full cells applied a 20-μm Li metal anode mounted on Cu foil purchased from China Energy Lithium Co. The full cells were finally assembled in CR-2016 coin cells with aluminum foil protection on the cathode side of the coin cell case, which has been shown to reduce oxidative reactivity of ether electrolytes (35). NCA || 20-μm Li pouch cells used 58 × 45 mm anodes and 57 × 44 mm cathodes, with all tabs and laminated films purchased from MTI.

Characterization. The morphology of the deposited Li metal at various temperatures was characterized using a FEI Quanta 250 scanning electron microscope (SEM). Cryo-FIB SEM was conducted in a Thermo Scientific Scios 2 DualBeam FIB/SEM. The images were taken at 5 kV in the SEM mode. NMR spectroscopy was conducted on a Varian Inova 500 MHz NMR spectrometer using an SW Probe tunable to O17 and Li7. XPS was carried out using a AXIS Supra by Kratos Analytical with an Al monochromatic anode source at 15 kV with a 5.0×10^{-8} Torr vacuum level. All the peaks were fitted based on the reference C–C bond at 284.6 eV. Raman spectroscopy was conducted on a Renishaw inVia Raman Microscope which utilized a 532-nm laser as an excitation source and a high-resolution 1,800 groove/mm grating. Detailed sample preparation and characterization methods are provided in *SI Appendix*.

Electrochemical Testing. All electrochemical data provided in this work were produced by CR-2032 and CR-2016 type coin cells assembled in an Ar-filled glove box kept at <0.5 ppm O_2 and <0.1 ppm H_2O. Coin cell cycling at low temperature was conducted inside SolidCold C4-76A and SolidCold C-186A ultralow chest freezers for −40 °C and −60 °C tests, respectively, whereas EIS measurements and pouch cell cycling were conducted in an ESPEC BTX-475 temperature chamber. The electrolyte conductivity values were obtained with EIS using the following equation: $\sigma = \frac{L}{A * R'}$ where R is the measured ionic resistance and A and L are the area of and space between the electrodes, respectively. Cells were rested for at least 2 h at low temperature to achieve equilibration. Low-temperature galvanostatic testing was done on an Arbin LBT-10V5A system, while room-temperature galvanostatic testing was done on a Neware BTS 4000 system. All potentiostatic tests were carried out on a Biologic VSP-300 potentiostat. Pouch cells were assembled in the glove box with cathode and anode dimensions of 57 × 44 mm and 58 × 45 mm, respectively. Detailed descriptions of the electrochemical testing methods and pouch cell assembly are provided in *SI Appendix*.

Molecular Simulations. Classical, fixed-charge MD simulations were performed in the Large-scale Atomic/Molecular Massively Parallel Simulator (LAMMPS) software, with the solvents and Li^+ described using the General Amber forcefield, while the anion was described with the potential of Gouveia et al. (61). The initial simulations cells were constructed using in-house scripts, with the salt ions randomly distributed in the solvent with compositions described in *SI Appendix*, Table S1. For the interfacial simulations, electrolytes were placed in contact with 2 hexagonal graphene sheets, described by the QMFF-Cx potential (62). Van der Waals interactions not explicitly specified in the forcefields were generated using Lorentz–Berthelot mixing rules (63). In all cases, the charges of the Li^+ and FSI^- molecules were scaled to the high-frequency dielectric properties of the solvents present in the system according to the method employed by Park et al. (64) which was 0.73 for LDME systems and 0.74 for LDEE. For bulk electrolytes (no interface), periodic boundary conditions were applied in all directions, while only in the x and y directions for the interfacial cells. Quantum chemistry simulations were performed using the Q-Chem 5.1 quantum chemistry package at the M06-HF//6-31+G(d, p) level of theory for geometry optimization and the M06-HF//6-311++G** level of theory for energy and vibrational analysis. A detailed description of the MD and MTD protocols is shown in *SI Appendix*.

Pouch Cell Energy Density Projections. The cell level energy densities for this work were calculated via the 18,650-cylinder cell model proposed by Betz et al. that we adapted for pouch-type configurations (59). Unless specified otherwise, the materials metrics (e.g., current collector thickness/density) from Betz et al. were used. A 30% cathode porosity and a 0% Li porosity were applied in the model. The cathode and anode dimensions were assumed to be 4.4 × 5.7 and 4.5 × 5.8 cm, respectively which matches the electrodes used in this work. The pouch cell film parameters and positive/negative tab masses were measured experimentally from products purchased from MTI. An N/P capacity ratio of 2 was assumed to match the loading demonstrated in this work. For each cathode loading, the number of cathode and anode layers was adjusted manually. The number of double-sided anodes, double-sided cathodes, and single-sided cathodes were taken as x, x-1, and 2, respectively. Enough pouch film to provide 20% extra stack thickness was assumed, which is generally required to provide enough area for sealing. For projections at each temperature, the specific capacity and average discharge voltage of the coin cells employing both electrolytes of interest were used (*SI Appendix*, Fig. S23). However, it was assumed that the loadings of each component were maintained based on the room-temperature performance so as to not inflate the low-temperature energy densities.

Data, Materials, and Software Availability. All study data are included in the article and/or supporting information.

ACKNOWLEDGMENTS. This work was supported by NASA Space Technology Graduate Research Opportunity 80NSSC20K1174. Part of the work used the University of California San Diego-MTI Corporation Battery Fabrication Facility and the UCSD-Arbin Battery Testing Facility. Electron microscopic characterization was performed at the San Diego Nanotechnology Infrastructure of UCSD, a member of the National Nanotechnology Coordinated Infrastructure, which is supported by the NSF (Grant ECCS-1542148). This work used the Expanse supercomputer at the San Diego Supercomputing center through allocation PHY200077 from the Advanced Cyberinfrastructure Coordination Ecosystem: Services & Support program, which is supported by NSF grants #2138259, #2138286, #2138307, #2137603, and #2138296. The authors also acknowledge Dr. Stephen Russell Lynch for assistance with the NMR experiments.

1. M. Armand, J.-M. Tarascon, Building better batteries. *Nature* **451**, 652–657 (2008).
2. S. Li *et al.*, Developing high-performance lithium metal anode in liquid electrolytes: Challenges and progress. *Adv. Mater.* **30**, 1706375 (2018).
3. J. Liu *et al.*, Pathways for practical high-energy long-cycling lithium metal batteries. *Nat. Energy* **4**, 180–186 (2019).
4. D. Lin, Y. Liu, Y. Cui, Reviving the lithium metal anode for high-energy batteries. *Nat. Nanotechnol.* **12**, 194–206 (2017).
5. S. Ahmed *et al.*, Enabling fast charging–A battery technology gap assessment. *J. Power Sources* **367**, 250–262 (2017).
6. W. Cai *et al.*, A review on energy chemistry of fast-charging anodes. *Chem. Soc. Rev.* **49**, 3806–3833 (2020).
7. Y. Liu, Y. Zhu, Y. Cui, Challenges and opportunities towards fast-charging battery materials. *Nat. Energy* **4**, 540–550 (2019).
8. M. Weiss *et al.*, Fast charging of lithium-ion batteries: A review of materials aspects. *Adv. Energy Mater.* **11**, 2101126 (2021).
9. N. Zhang *et al.*, Critical review on low-temperature Li-ion/metal batteries. *Adv. Mater.* **34**, 2107899 (2022).
10. A. Gupta, A. Manthiram, Designing advanced lithium-based batteries for low-temperature conditions. *Adv. Energy Mater.* **10**, 2001972 (2020).
11. D. Hubble *et al.*, Liquid electrolyte development for low-temperature lithium-ion batteries. *Energy Environ. Sci.* **15**, 550–578 (2022).
12. K. Xu, A. von Cresce, U. Lee, Differentiating contributions to "ion transfer" barrier from interphasial resistance and Li^+ desolvation at electrolyte/graphite interface. *Langmuir* **26**, 11538–11543 (2010).
13. K. Xu, "Charge-transfer" process at graphite/electrolyte interface and the solvation sheath structure of Li[Sup +] in nonaqueous electrolytes. *J. Electrochem. Soc.* **154**, A162 (2007).
14. Q. Li *et al.*, Li^+-desolvation dictating lithium-ion battery's low-temperature performances. *ACS Appl. Mater. Interfaces* **9**, 42761–42768 (2017).
15. E. R. Logan, J. R. Dahn, Electrolyte design for fast-charging li-ion batteries. *Trends Chem.* **2**, 354–366 (2020).
16. E. R. Logan *et al.*, Ester-based electrolytes for fast charging of energy dense lithium-ion batteries. *J. Phys. Chem. C* **124**, 12269–12280 (2020).
17. M. C. Smart, B. V. Ratnakumar, K. B. Chin, L. D. Whitcanack, Lithium-ion electrolytes containing ester cosolvents for improved low temperature performance. *J. Electrochem. Soc.* **157**, A1361–A1374 (2010).
18. M. C. Smart, B. V. Ratnakumar, S. Surampudi, Use of organic esters as cosolvents in electrolytes for lithium-ion batteries with improved low temperature performance. *J. Electrochem. Soc.* **149**, A361–A370 (2002).
19. M. C. Smart *et al.*, Gel polymer electrolyte lithium-ion cells with improved low temperature performance. *J. Power Sources* **165**, 535–543 (2007).
20. X. Fan *et al.*, Non-flammable electrolyte enables Li-metal batteries with aggressive cathode chemistries. *Nat. Nanotechnol.* **13**, 715 (2018).
21. X. Fan *et al.*, Highly fluorinated interphases enable high-voltage Li-metal batteries. *Chem* **4**, 174–185 (2018).
22. J. Alvarado *et al.*, Bisalt ether electrolytes: A pathway towards lithium metal batteries with Ni-rich cathodes. *Energy Environ. Sci.* **12**, 780–794 (2019).
23. B. Liao *et al.*, Designing low impedance interface films simultaneously on anode and cathode for high energy batteries. *Adv. Energy Mater.* **8**, 1800802 (2018).
24. S. Chen *et al.*, High-voltage lithium-metal batteries enabled by localized high-concentration electrolytes. *Adv. Mater.* **30**, 1706102 (2018).
25. E. Markevich, G. Salitra, D. Aurbach, Fluoroethylene carbonate as an important component for the formation of an effective solid electrolyte interphase on anodes and cathodes for advanced Li-ion batteries. *ACS Energy Lett.* **2**, 1337–1345 (2017).
26. S. S. Zhang, K. Xu, T. R. Jow, The low temperature performance of Li-ion batteries. *J. Power Sources* **115**, 137–140 (2003).
27. S. S. Zhang, K. Xu, T. R. Jow, Electrochemical impedance study on the low temperature of Li-ion batteries. *Electrochim. Acta* **49**, 1057–1061 (2004).
28. J. Holoubek *et al.*, Tailoring electrolyte solvation for Li metal batteries cycled at ultra-low temperature. *Nat. Energy* **6**, 303–313 (2021).
29. J. Holoubek *et al.*, Electrolyte design implications of ion-pairing in low-temperature Li metal batteries. *Energy Environ. Sci.* **15**, 1647–1658 (2022).
30. J. Holoubek *et al.*, Predicting the ion desolvation pathway of lithium electrolytes and their dependence on chemistry and temperature. *J. Phys. Chem. Lett.* **13**, 4426–4433 (2022).
31. X. Fan *et al.*, All-temperature batteries enabled by fluorinated electrolytes with non-polar solvents. *Nat. Energy* **4**, 882–890 (2019).
32. H. Cheng *et al.*, Emerging era of electrolyte solvation structure and interfacial model in batteries. *ACS Energy Lett.* **7**, 490–513 (2022).
33. J. Xu *et al.*, Electrolyte design for Li-ion batteries under extreme operating conditions. *Nature* **614**, 694–700 (2023).
34. Y.-X. Yao *et al.*, Regulating interfacial chemistry in lithium-ion batteries by a weakly solvating electrolyte. *Angew. Chem. Int. Ed. Engl.* **60**, 4090–4097 (2021).
35. X. Ren *et al.*, Enabling high-voltage lithium-metal batteries under practical conditions. *Joule* **3**, 1662–1676 (2019).
36. H. Liu *et al.*, Ultrahigh coulombic efficiency electrolyte enables Li||SPAN batteries with superior cycling performance. *Mater. Today* **42**, 17–28 (2020).
37. J. Qian *et al.*, High rate and stable cycling of lithium metal anode. *Nat. Commun.* **6**, 6362 (2015).
38. X. Cao *et al.*, Optimization of fluorinated orthoformate based electrolytes for practical high-voltage lithium metal batteries. *Energy Storage Mater.* **34**, 76–84 (2021).
39. X. Dong *et al.*, High-energy rechargeable metallic lithium battery at −70 °C enabled by a cosolvent electrolyte. *Angew. Chem. Int. Ed. Engl.* **58**, 5623–5627 (2019).
40. D. Aurbach, O. Youngman, Y. Gofer, A. Meitav, The electrochemical behaviour of 1,3-dioxolane–$LiClO_4$ solutions–I. Uncontaminated solutions. *Electrochim. Acta* **35**, 625–638 (1990).
41. B. D. Adams, J. Zheng, X. Ren, W. Xu, J.-G. Zhang, Accurate determination of coulombic efficiency for lithium metal anodes and lithium metal batteries. *Adv. Energy Mater.* **8**, 1702097 (2018).
42. S. Kuang *et al.*, Anion-containing solvation structure reconfiguration enables wide-temperature electrolyte for high-energy-density lithium-metal batteries. *ACS Appl. Mater. Interfaces* **14**, 19056–19066 (2022).
43. C.-B. Jin *et al.*, Taming solvent-solute interaction accelerates interfacial kinetics in low-temperature lithium-metal batteries. *Adv. Mater.* **35**, 2208340 (2023).
44. S. Kim, V. G. Pol, Tailored solvation and interface structures by tetrahydrofuran-derived electrolyte facilitates ultralow temperature lithium metal battery operations. *ChemSusChem* **16**, e202202143 (2023).
45. J. Wang *et al.*, Superconcentrated electrolytes for a high-voltage lithium-ion battery. *Nat. Commun.* **7**, 12032 (2016).
46. Y. Yamada, J. Wang, S. Ko, E. Watanabe, A. Yamada, Advances and issues in developing salt-concentrated battery electrolytes. *Nat. Energy* **4**, 269–280 (2019), 10.1038/s41560-019-0336-z.
47. M. A. Danzer, Generalized distribution of relaxation times analysis for the characterization of impedance spectra. *Batteries* **5**, 53 (2019).
48. R. Jorn, L. Raguette, S. Peart, Investigating the mechanism of lithium transport at solid electrolyte interphases. *J. Phys. Chem. C* **124**, 16261–16270 (2020).
49. R. Jorn, R. Kumar, D. P. Abraham, G. A. Voth, Atomistic modeling of the electrode-electrolyte interface in Li-ion energy storage systems: Electrolyte structuring. *J. Phys. Chem. C* **117**, 3747–3761 (2013).
50. A. Baskin, D. Prendergast, "Ion solvation spectra": Free energy analysis of solvation structures of multivalent cations in aprotic solvents. *J. Phys. Chem. Lett.* **10**, 4920–4928 (2019).
51. A. Baskin, D. Prendergast, Ion solvation engineering: How to manipulate the multiplicity of the coordination environment of multivalent ions. *J. Phys. Chem. Lett.* **11**, 9336–9343 (2020).
52. A. Baskin, J. W. Lawson, D. Prendergast, Anion-assisted delivery of multivalent cations to inert electrodes. *J. Phys. Chem. Lett.* **12**, 4347–4356 (2021).
53. A. Barducci, M. Bonomi, M. Parrinello, Metadynamics. *WIREs Comput. Mol. Sci.* **1**, 826–843 (2011).
54. Y. M. Cahen, P. R. Handy, E. T. Roach, A. I. Popov, Spectroscopic studies of ionic solvation. XVI. Lithium-7 and Chlorine-35 nuclear magnetic resonance studies in various solvents. *J. Phys. Chem.* **79**, 80–85 (1975).
55. D. T. Boyle *et al.*, Transient voltammetry with ultramicroelectrodes reveals the electron transfer kinetics of lithium metal anodes. *ACS Energy Lett.* **5**, 701–709 (2020).
56. K. Kondo *et al.*, Conductivity and solvation of Li^+ ions of $LiPF_6$ in propylene carbonate solutions. *J. Phys. Chem. B* **104**, 5040–5044 (2000).
57. M. Castriota *et al.*, Temperature dependence of lithium ion solvation in ethylene carbonate–$LiClO_4$ solutions. *J. Chem. Phys.* **118**, 5537–5541 (2003).
58. Y. Chae *et al.*, Lithium-ion solvation structure in organic carbonate electrolytes at low temperatures. *J. Phys. Chem. Lett.* **13**, 7881–7888 (2022).
59. J. Betz *et al.*, Theoretical versus practical energy: A plea for more transparency in the energy calculation of different rechargeable battery systems. *Adv. Energy Mater.* **9**, 1803170 (2019).
60. J. Holoubek, Z. Chen, P. Liu, Application-based prospects for dual-ion batteries. *ChemSusChem* **16**, e202201245 (2023).
61. A. S. L. Gouveia *et al.*, Ionic liquids with anions based on fluorosulfonyl derivatives: From asymmetrical substitutions to a consistent force field model. *Phys. Chem. Chem. Phys.* **19**, 29617–29624 (2017).
62. T. A. Pascal, N. Karasawa, W. A. Goddard, Quantum mechanics based force field for carbon (QMFF-Cx) validated to reproduce the mechanical and thermodynamics properties of graphite. *J. Chem. Phys.* **133**, 134114 (2010).
63. H. A. Lorentz, Ueber die Anwendung des Satzes vom Virial in der kinetischen Theorie der Gase. *Ann. Phys.* **248**, 127–136 (1881).
64. C. Park *et al.*, Molecular simulations of electrolyte structure and dynamics in lithium-sulfur battery solvents. *J. Power Sources* **373**, 70–78 (2018).